Mechanisms Responsible for ω-Pore Currents in Ca$_V$ Calcium Channel Voltage-Sensing Domains

Stefania Monteleone,[1] Andreas Lieb,[2,3] Alexandra Pinggera,[2,4] Giulia Negro,[2] Julian E. Fuchs,[1] Florian Hofer,[1] Jörg Striessnig,[2] Petronel Tuluc,[2,*] and Klaus R. Liedl[1,*]

[1]Institute of General, Inorganic and Theoretical Chemistry and [2]Department of Pharmacology and Toxicology, Center for Molecular Biosciences, University of Innsbruck, Innsbruck, Austria; [3]Institute of Neurology, University College London, London, United Kingdom; and [4]Neurobiology Division, MRC Laboratory of Molecular Biology, Cambridge, United Kingdom

ABSTRACT   Mutations of positively charged amino acids in the S4 transmembrane segment of a voltage-gated ion channel form ion-conducting pathways through the voltage-sensing domain, named ω-current. Here, we used structure modeling and MD simulations to predict pathogenic ω-currents in Ca$_V$1.1 and Ca$_V$1.3 Ca^{2+} channels bearing several S4 charge mutations. Our modeling predicts that mutations of Ca$_V$1.1-R1 (R528H/G, R897S) or Ca$_V$1.1-R2 (R900S, R1239H) linked to hypokalemic periodic paralysis type 1 and of Ca$_V$1.3-R3 (R990H) identified in aldosterone-producing adenomas conducts ω-currents in resting state, but not during voltage-sensing domain activation. The mechanism responsible for the ω-current and its amplitude depend on the number of charges in S4, the position of the mutated S4 charge and countercharges, and the nature of the replacing amino acid. Functional characterization validates the modeling prediction showing that Ca$_V$1.3-R990H channels conduct ω-currents at hyperpolarizing potentials, but not upon membrane depolarization compared with wild-type channels.

INTRODUCTION

High voltage-gated Ca^{2+} channels are transmembrane protein complexes of a pore-forming α_1-, an extracellular $\alpha_2\delta$-, and an intracellular β-subunit (1). Although the pore-forming subunit of the K$^+$ channels and bacterial Na$^+$ channels are homotetrameric assemblies, all four repeats of the mammalian Ca^{2+} or Na$^+$ channels are encoded by a single gene allowing for structural and functional diversity of the repeats (2,3). Each repeat of the voltage-gated Ca^{2+} channel consists of six transmembrane helices with the S1−S4 forming the voltage-sensing domain (VSD), and the S5 and S6 segments plus their connecting S5 and S6 linkers form the actual channel pore. Four to six positively charged amino acids Arg (R) and Lys (K) located in the S4 transmembrane segments at every turn of the helical structure confer the VSD with its ability to detect changes in the membrane potential. Although the movement of the S4 helices has been a matter of debate, the current consensus based on crystallographic data is that they move along a clockwise spiral path toward the extracellular side of the membrane through a water-filled gating pore (4–6). The translocation of the S4 segment transmitted through S4

and S5 linkers induces a conformational change of the S5 and S6 pore-lining domains, triggering the opening of the cytoplasmic activation gate. The translocation of the S4 helix through the hydrophobic milieu of the lipid bilayer is a thermodynamically unfavorable process. Therefore, the movement of the S4 segment is aided by transient hydrogen bonds (H-bonds) formed between the side chains of the positively charged S4 amino acids and negatively charged side chains (countercharges) in the S1–S3 segments. The presence of water-filled cavities on the extracellular and intracellular sides of the gating pore also aids the neutralization of the S4 charges, and furthermore helps focus the electrical field across a narrow region of the VSD. Nevertheless, the two water vestibules need to be physically separated to avoid ion transfer, because an uncontrolled ion flux through the membrane can change membrane excitability and ion homeostasis as revealed by human disease-causing mutations (7,8). Therefore, a critical structural feature of the VSD is the presence of a "hydrophobic plug," formed by one Phe ring positioned in the central plane of the lipid bilayer that separates the outer and inner water-filled vestibule of the gating pore, thus blocking the ion transfer through the VSD (9,10).

A special class of human channelopathies results from mutations of charged S4 amino acids to small hydrophilic residues (1). Because the charged S4 residues confer voltage

---

CrossMark

sensitivity to the VSD, the neutralization of S4 gating charges can not only reduce the voltage sensitivity of ionic current passing through the canonical α-conduction pore (11–13), but may also create a secondary ion-conducting pathway through the affected VSD, a so-called ω-current or gating-pore current. In the last decade, ω-currents have been experimentally measured in K^+ ($K_V1.2$ and Shaker), Na^+ ($Na_V1.2$, $Na_V1.4$, $Na_V1.5$, and NaChBac) (14–20), and proton channels (21,22). Development of ω-currents is voltage-dependent, as they appear in the conformational state of the VSD, where the position of the missing charge is right above or below the hydrophobic plug (23). Neutralization of the uppermost S4 charges induces ω-currents with the VSD in the resting state, whereas mutations of the innermost residues results in ω-currents upon VSD activation. Although most of the charge mutations create selective (24) or nonselective cation (16,25) ω-currents, their mutation to His (H) results in proton currents, as protons are transferred via a Grotthuss hopping mechanism through the H-bond network of water molecules (a so-called water wire) filling the gating pore (14,26).

Several mutations of S4 charges have also been identified for Ca^{2+} channels, but ω-pore currents have been measured only for one of them (27). These mutations leading to hypokalemic periodic paralysis (HypoPP) occur in the $Ca_V1.1$ channel at R1 position in the II repeat (R528), and R2 position in the IV repeat (R1239) (28,29). ω-pore currents have also been proposed for R897S and R900S mutants, which constitute the R1 and R2 gating charges in the third repeat of the $Ca_V1.1$ channel (30). Several pathogenic mutations of gating charges in the $Ca_V2.1$ leading to Familial Hemiplegic Migraine type 1 (31–34), and $Ca_V1.3$ channels causing excessive aldosterone secretion in aldosterone-producing adenomas (APAs) (35) have been described but, to date, the difficult measurement of the ω-currents in these channels has not been attempted. With the advent of genetic studies, the number of disease-related ion channel mutations have dramatically increased, yet the functional characterization of these mutations falls behind. In recent years, computational techniques such as molecular modeling and MD simulations have proved to be essential tools in ion channel research to provide valuable structural information regarding the ion channel function, and to help predict functional alterations induced by mutations (36–41).

Here, we present structural models of several VSDs containing five disease-causing mutations in $Ca_V1.1$ and one mutation in $Ca_V1.3$ S4 transmembrane segments in different gating states, and analyzed the occupancy of the gating pore by water molecules, a prerequisite for ω-currents. Our modeling demonstrates the occurrence of water wires in several gating states of all mutated but not in wild-type (WT) VSDs. The detailed analysis shows the effect of S4 charge mutation on the H-bond interactions within the VSD, and the destabilizing effects of S4 charge mutations on S3 or S4 helical structures that result in increased size

of the ω-gating pore. To validate our modeling prediction, we experimentally show the appearance of state-dependent ω-currents in $Ca_V1.3$-R3H channels.

MATERIALS AND METHODS

Structure modeling

For the homology modeling of the human $Ca_V1.1$ α_1-subunit we used as template the cryo-EM structure of the rabbit $Ca_V1.1$ in the gated but inactivated state (PDB: 3jbr (42)). The sequence similarity between human and rabbit isoform is very high and allows us to build a reliable model. We modeled the human $Ca_V1.3$ α_1-subunit based on the human $Ca_V1.1$ model. Sequences were aligned with ClustalW (43). By shifting the S4 sequence alignment toward the C-terminus by three and six residues, we generated the "resting state α" and "resting state β," respectively (19).

Homology modeling has been performed using the respective tools in MOE (Molecular Operating Environment, version 2015.1001 (44)), a multifunctional application used in molecular modeling, using the Amber12 force field (45) and default settings. The C-terminus and N-terminus parts were capped using acetyl and N-methyl groups to avoid perturbations by free charged functional groups.

Ab initio modeling of loops

Because the loop sequences are not conserved among ion channels, we used ab initio modeling to rebuild them from the homology model. In particular, we used either dedicated MOE tools or the Rosetta method (46). For $Ca_V1.1$, we modeled the long $Ca_V1.1a$ splice variant (47).

Modeling of mutant VSDs

We modeled six mutants for $Ca_V1.1$ (R1 in II repeat (R528H (R1H) and R528G (R1G)), R1 (R897S (R1S)) and R2 (R900S (R2S)) in III repeat, and R2 in IV repeat (R1239H (R2H) and R1239G)) and one mutation for R3 in III repeat of $Ca_V1.3$ channel (R990H (R3H)). The structures of single mutants were derived from the respective WT VSD models by replacing the residue that was involved in the mutation and carrying out a local energy minimization with MOE.

MD simulations

Models were embedded in membranes containing 1-palmitoyl-2-oleoyl-sn-glycero-3-phosphocholine and cholesterol in a ratio of 3:1, using the CHARMM-GUI Membrane Builder (48). The z axis was aligned along the main axis of the protein that, in all cases, corresponded to the ω-pore. The simulation box (with x and y axes of 80 Å) included a 17.5 Å layer of water molecules (TIP3P model (49)) and ions (150 mM calcium chloride or potassium chloride). We then performed an energy minimization step: starting coordinates and topology were generated by the LeaP tool of Amber14, using dedicated force fields for proteins and lipids, ff14SBonlysc (50) and Lipid14, respectively (51).

The system was gradually heated from 100 to 300 K (regulated using the Langevin thermostat) and then equilibrated over 1 ns in anisotropic pressure-scaling conditions (using the Berendsen barostat, at the pressure of 1 bar), which is suitable for membrane proteins. MD simulations were performed at 300 K for at least 100 ns, until convergence, with a 2-fs time step. For $Ca_V1.3$ VSD, the sampling was extended up to 1 μs to prove the stability of the water wire in the mutant protein (Fig. S4). Van der Waals and short-range Coulomb interactions were cut off at 10 Å, whereas long-range electrostatics were calculated through the particle mesh Ewald

method (52). All His residues were modeled in the uncharged state with the ε-protonated nitrogen.

MD runs were carried out using the GPU implementation of pmemd (52). Trajectories were analyzed through CPPTRAJ Amber15 tools (53) and visualized with VMD (version 1.9.1 (54)). The identification of key interactions was aided by other visualization tools, such as MOE and PyMOL (version 1.6 (55)). To quantify the number of water molecules in WT and mutant VSDs, we calculated water-density profiles. We considered the positions of water molecules along the z axis perpendicular to the membrane plane over 100 ns simulations; the center of the box was defined as Cζ atom of the conserved Phe residue. We also analyzed the positions of gating charges, defined as the Cζ atom in the WT R residues, and Nε2, Cα, and Oγ for H, G, and S mutants, respectively. Afterwards, we averaged the number of water molecules over 2000 snapshots periodically extracted over 100 ns, and plotted it using Gnuplot tools (version 5.0 (56)).

Functional characterization: complementary cDNA constructs

The human WT Ca$_V$1.3 α_1-subunit construct (EU363339, long C-terminus splice variant containing alternative exon 8a) was previously cloned into pGFP^{minus} vector (no GFP tag, cytomegalovirus promoter) (57). Mutation R3H was introduced into the human WT Ca$_V$1.3 construct using standard polymerase chain reaction approaches and verified by DNA sequencing (Eurofins Genomics, Ebersberg, Germany).

Functional characterization: electrophysiological recordings in tsA-201 cells

tsA-201 cells were maintained in culture and transiently transfected with WT or mutant Ca$_V$1.3 α_1-, and auxiliary β3- (NM_012828) and $\alpha_2\delta$-1- (NM_001082276) subunits, as previously described (58). For whole-cell patch-clamp recordings, borosilicate glass electrodes (64-0792, Harvard Apparatus) were pulled (P-1000; Sutter Instruments, Novato, California) and fire-polished (MF-830 Microforge; Narashige, London, United Kingdom) at a final resistance of 1.5–2.5 MΩ. Recordings were performed with an Axopatch 200B amplifier (Molecular Devices, Biberach, Germany), digitized with a Digitizer 1322A (Molecular Devices), and low-pass filtered at 5 kHz. Recordings showing currents smaller than 100 pA were excluded from analysis. Compensation was applied for 60% of the series resistance. The internal solution contained the following: 135 mM cesium chloride, 10 mM N-2-hydroxyethylpiperazine-N-2-ethanesulfonic acid, 10 mM cesium-ethylene glycol tetraacetic acid, 1 mM magnesium chloride, 4 mmol/L disodium adenosine 5′-triphosphate (adjusted to pH 7.4 with cesium hydroxide); bath solution: 15 mM Ca^{2+} chloride, 10 mM N-2-hydroxyethylpiperazine-N-2-ethanesulfonic acid, 150 mM choline chloride, and 1 mM magnesium chloride (adjusted to pH 7.4 with cesium hydroxide). For determining the current-voltage relationship, a 50-ms-long step protocol starting from a holding potential of −80 mV to different voltages was applied. Resulting I-V curves were analyzed as previously described (59). To investigate the channel surface expression, we analyzed the integrated Q$_{ON}$-gating currents at reversal potential. Leak subtraction was performed online using the P/4 protocol. Recordings were junction potential corrected by subtracting 9.3 mV (59). To measure ω-currents, the cell was depolarized from −120 to 20 mV in 20-mV increments. First, the bath solution contained 150 mM choline chloride and 15 mM Ca^{2+} chloride to inactivate Ca^{2+} currents. Immediately after the steady-state inactivation was reached, the solution was exchanged to 165 mM guanidinium chloride without Ca^{2+} chloride, to measure the guanidinium conductance. The ω-current was calculated as the difference between remaining current at the end of the Ca^{2+} current steady-state inactivation and the current elicited in the presence of guanidinium chloride.

Statistics

Data were analyzed using Clampfit 10.2 (Axon Instruments), SigmaPlot 12.5 (Systat Software), and GraphPad Prism 5 software (GraphPad). All values are presented as mean $\pm$ SE for the indicated number of experiments (n). Data were analyzed by unpaired Student's t-test and Mann-Whitney test when not normally distributed. Statistical significance was set at $p < 0.05$.

RESULTS

Cav1.1 R1H and R1G form water wires in the resting state α

Previously it has been shown in homotetrameric voltage-gated Na$^+$ and K$^+$ channels that if the R1 gating charge is mutated, the VSD conducts an ω-current in the resting state α (20,60). To test whether R1 mutation in the II repeat of Ca$_V$1.1 changes the occupancy of the gating pore by water molecules, we generated structure models of WT VSD and the HypoPP mutations R1H and R1G in the resting state α, where the R1 position is just above the Phe hydrophobic plug (Fig. 1). The models were stable over 100 ns of MD simulations: the root mean-square deviation to the starting structure is $\sim$3 Å for all C$_\alpha$ atoms, 1.5–2 Å for transmembrane residues, and 3–4 Å for all atoms (side chains included) (Figs. S1–S4). Helices were stable in the WT VSDs, where occupancy values are high, especially for α-helices ($\sim$90%) (Table S5). In the WT structure, the center of the VSD was sealed by two gating charges, R1 and R2 (R528 and R531), that form ionic interactions with the countercharges E452 (in the S1 and S2 extracellular loop) and E2 (E478 in the S2 helix), respectively (Fig. 1 A; Table S4). H-bonds with E452 had an average length of 2.98 $\pm$ 0.23 Å and were stable over the entire simulation time. D3 (D500 in S3) interacted mainly with water molecules and E4 (E510 in S3) interacted mainly with R469, an additional Arg residue in helix S2. The distance between E4 and R469 was in the range 2.63–6.00 Å, whereas the distance to R1 heavy side-chain atoms was always larger than 7 Å, indicating that E4 does not form any interactions with R1. In the absence of any structure constrains, de novo modeling of linkers can yield very divergent results. Because the MD simulations show that the extracellular water-filled vestibule in the WT VSD is sealed by the R1-E452 interaction, we tested whether, in the absence of the extracellular S1 and S2 linker, the WT VSD can form a water wire. Modeling the WT VSD without extracellular or intracellular linkers (Fig. S6) showed that in the absence of E452, R1 side chain reorients and interacts with E4. This demonstrates that the interaction of R1 with any countercharge is necessary for sealing the hydrophobic core of the WT VSD.

The substitution of R1 with the shorter side chain of His increased the free space in the upper part of the protein, and His did not form ionic interactions with the negative countercharge in the extracellular loop (Fig. 1 B). H-bonds
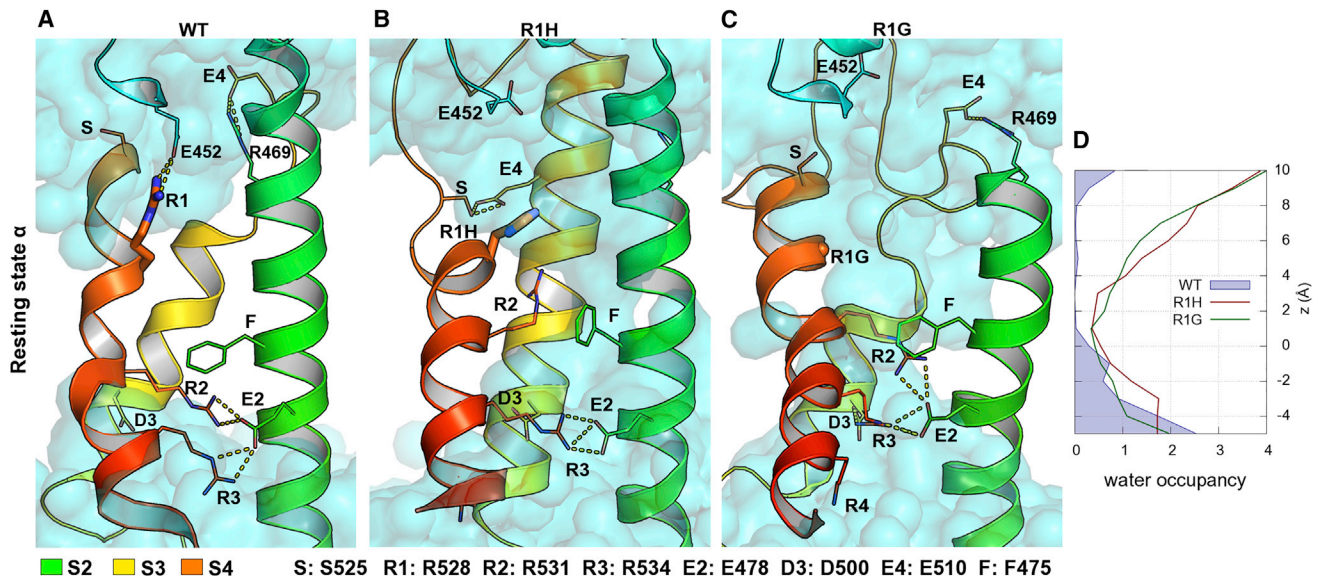
FIGURE 1 Mutation of R1 residue to His or Gly increases the water occupancy in VSD II of Ca$_v$1.1 channel in resting state α. (A). Representative cluster of the WT VSD. The center of the VSD is water sealed by R1 (R528) above the conserved F residue of helix S2. R2 and R3 are below, forming ionic interactions with E2. (B) Top cluster of R1H mutated VSD. His has a shorter side chain compared with Arg, allowing water molecules (cyan) to enter the voltage sensor. R2 side chain moves upwards and forms H-bonds with water molecules. R0 interacts with E4 stabilizing the helical structure of S3. (C) Mutating R1 to Gly also increases the free space in the upper part of the protein facilitating the formation of the water wire. Due to the lack of interactions, S3 loses more of its helical structure compared with WT. (D) Water occupancy in mutants and WT VSDs. The plot shows that a larger number of water molecules occupy the center of the VSD in both R1H and R1G mutants compared with WT. To see this figure in color, go online.

between R1H and E452 of the S1 and S2 loop had a longer average distance compared with the WT (3.66 ± 1.07 Å between heavy atoms of acceptor and donor in the mutant), and were often replaced by interactions with water molecules. Moreover, Figs. 1 B and 4 A clearly show that the C$_\zeta$ atom of the R2 side chain moves by 4 Å upward into an active-like state, and R3 takes its role in the interaction with E2 and D3. Therefore, R1H and R2 guide water molecules toward the center of the VSD.

HypoPP mutation of the same R1 residue to Gly caused both the lack of a gating charge and a conformational change of the VSD. Similarly, as seen for the R1H VSD, the R2 C$_\zeta$ atom moved upward in an active-like state, but the shift was smaller than 3 Å (Fig. 1 C). The R2 side chain is closer to Phe in the center and still forms ionic interactions with its countercharge E2. However, the H-bond length increased from 2.79 ± 0.11 Å in the WT to 3.48 ± 0.97 Å in the mutant. Moreover, the structural model showed that the S3 segment partially loses some of the WT helical secondary structure, allowing more water molecules to pass through the VSD. Indeed, S3 in R1G VSD exhibits ~30% helical conformation over 100 ns of MD simulation, compared with 56% for the WT and 58% for the R1H VSD (Fig. S5 A; Table S5).

Both mutations generate continuous water wires in the center of the VSD over 100 ns simulation time (in the range −3 to +10 Å along the z axis), with 21.93 ± 1.12 water molecules for R1H and 19.39 ± 1.13 for R1G, compared with 3.90 ± 0.34 for the WT model (Fig. 1 D; Table 1).

Cav1.1 R1S and R2S form water wires in different resting states

To test whether mutation of R1 (R1S) or R2 (R2S) to Ser in III repeat of the Ca$_v$1.1 channel (30) leads to state-dependent ω-currents, we modeled the VSD in the resting states α and β. In the resting state α, R1 is oriented upwards together with R0, whereas R2 is placed below the conserved Phe residue together with R3 (Fig. 2 A). In our MD simulations, only one water molecule reached the center of the WT VSD, but it did not cause a water wire because both R1 and R2 lock the central hydrophobic constriction by interacting with the countercharges D1, and E2, D3, respectively (Fig. 2 A; Table S4). In resting state β of the WT VSD

TABLE 1 Integrated Water Occupancy and SD over 100 ns in the Center of VSD in Different Conformational States

Channel			State	Water Occupancy
Cav1.1	domain II	WT	resting α	3.90 ± 0.34
		R1H		21.93 ± 1.12
		R1G		24.24 ± 1.42
	domain III	WT	resting α	2.34 ± 0.24
			resting β	8.16 ± 0.46
		R1S	resting α	15.67 ± 0.54
		R2S	resting β	11.21 ± 0.63
	domain IV	WT	resting β	4.29 ± 0.37
		R2H		7.55 ± 0.55
Cav1.3	domain III	WT	resting β	0.89 ± 0.07
		R3H		7.28 ± 0.70

The calculation is performed along the z axis between R1 and R2 C$_\zeta$ atoms.
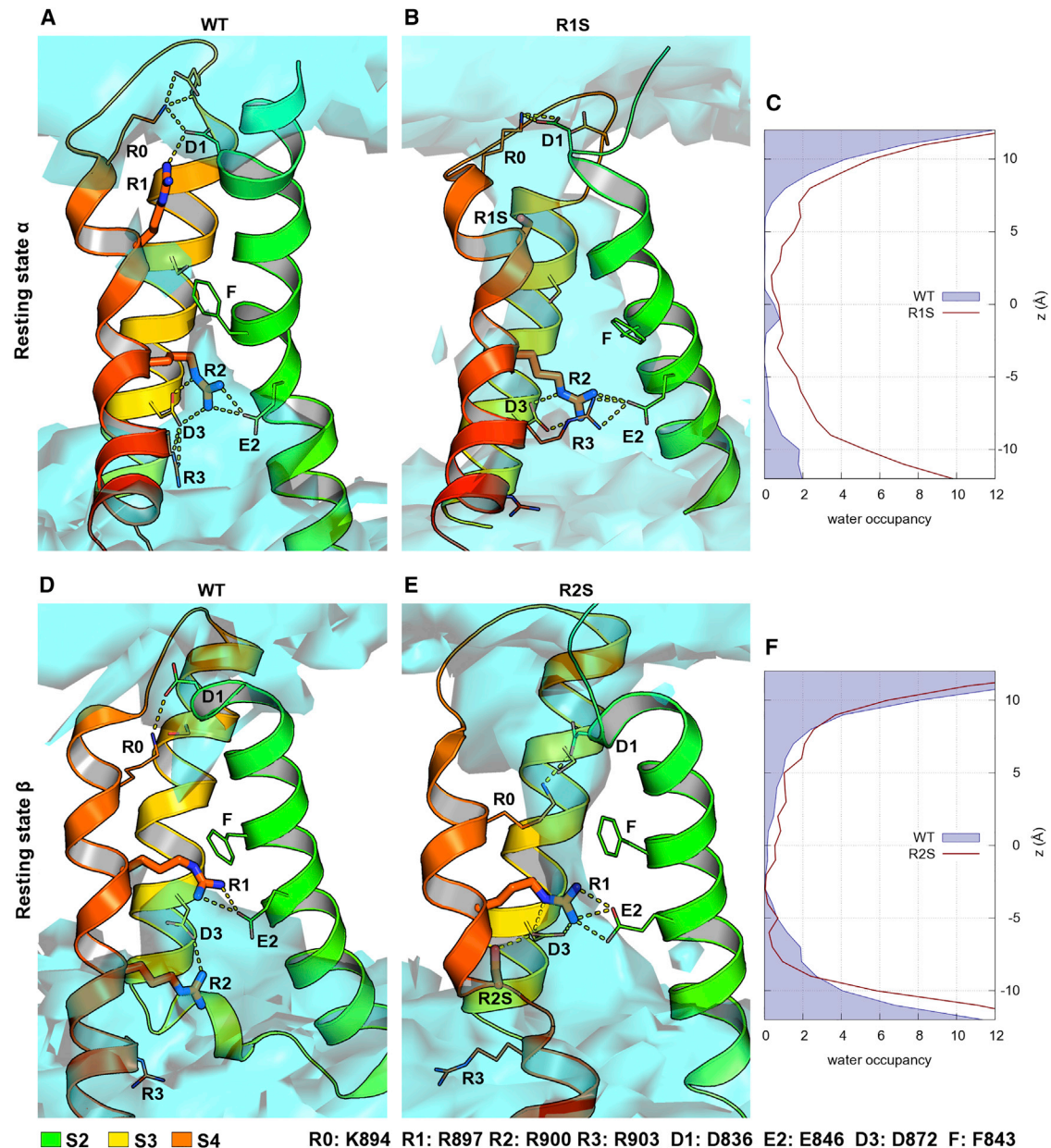
FIGURE 2 Mutation of R1 or R2 residues to Ser increases the water occupancy of VSD III of Ca$_V$1.1 channel in two distinct gating states. (*A*) Top cluster of WT VSD in resting state α. R1 interacts with D1 and R2 with E2, thus sealing the hydrophobic core of the VSD from the outer and inner water-filled vestibules respectively. (*B*) Mutation of R1 residue to Ser increases the space in the extracellular side of the VSD, allowing water (*cyan*) to reach the inner vestibule. (*C*) R1S VSD has a higher number of water molecules over the entire z axes compared with WT. (*D*) Top cluster of WT VSD in resting state β. The interactions of R1-E2 and R2-D3 stabilize the S4 helical structure and help to seal the hydrophobic core of the VSD. (*E*) After the mutation of R2 to Ser, the S4 helical structure is destabilized, allowing water to fill the hydrophobic constriction pore. (*F*) The R2S VSD has a higher number of water molecules in the center of the voltage sensor compared with the WT. To see this figure in color, go online.

(Fig. 2 *D*), the R0 charge is oriented upwards interacting with D1, whereas R1 moves downwards to interact with the E2 countercharge. Thus, R0 and R1 close the hydrophobic center, preventing water molecules from entering from either the extracellular or intracellular side. Mutating the R1 charge to Ser generated a water wire in the resting state α of the VSD due to the lack of a gating charge and the increased free space given by the smaller side chain of

S residue, with respect to R (Fig. 2 *B*). Ser still presents a potential H-bond donor and acceptor functional group and forms interactions with water molecules. R0 and R2 maintained their locations and ionic interactions with the countercharges. The water density analysis clearly showed that R1S creates a continuous water wire through the VSD, as the number of water molecules per frame increased from 2.34 ± 0.24 for the WT to 15.67 ± 0.54 for the mutant

(in the range −6 to +7 Å along the z axis) (Fig. 2 C; Table 1). Additionally, the mutation of R1 to Ser decreased the S4 helical structure occupancy to 59% compared with 76% for WT VSD, also increasing the probability that water occupies the gating pore (Fig. S5; Table S5). However, no water wires occurred in the resting state β of R1S because Ser cannot form any H-bonds with water molecules, but interacts with the backbone of S4, forming H-bonds that are conserved in helical secondary structure elements (Fig. S7 A). The S4 helix underwent a conformational change, forming a kink at the R2 level presenting lower helical secondary structure occupancy compared with the WT because R2 interacts with the E2 countercharge.

In the resting state α of the R2S model, R1 is still oriented upwards, whereas R2S is close to the conserved Phe residue and loses the interaction with countercharges in S2 and S3 (Fig. S7 B; Table S6). Nevertheless, no water wire was formed as the R2 interactions were replaced by R3. Instead, the R2S mutation resulted in a water wire in the resting state β because R2S reduced the hydrophobic constriction compared with WT VSD. The Ser at the R2 position maintained the interaction with D3 through an H-bond that replaces the ionic interaction and causes the break of helical secondary structure of S4 (Fig. 2 E; Tables S5 and S6).

Consequently, water can enter the VSD from the cytosolic side and the water density analysis indicates that the number of water molecules increased from 8.16 ± 0.46 for the WT to 11.21 ± 0.63 for the mutant (Fig. 2 F; Table 1).

Cav1.1 R2H forms a water wire in the resting state β

Similar to the III VSD, mutation of the R2 charge in the IV VSD of the Ca$_V$1.1 channel increased water occupancy when the VSD was in the resting state β. In the WT channel, the R0 (R1229) residue formed interactions with negatively charged amino acids in the extracellular loops and with D4 (D1196) (Fig. 3 A). Also, the gating charge R1 (R1236) stabilized the resting state by forming not only ionic interactions with D4, but also several H-bonds with other polar residues, such as T1158, S1193, and N1154 (2). R2 (R1239) formed ionic interactions with the other two countercharges, E2 (E1154) and D3 (D1186) of helices S2 and S3, respectively (Table S4). Because the R1 and R2 charges surround the Phe residues F1161 and F1157, their positions differ from the same state in III repeat and they orient as in the resting state α of the III VSD. The reason is that R0 in the IV VSD is at position −6 instead of −3.
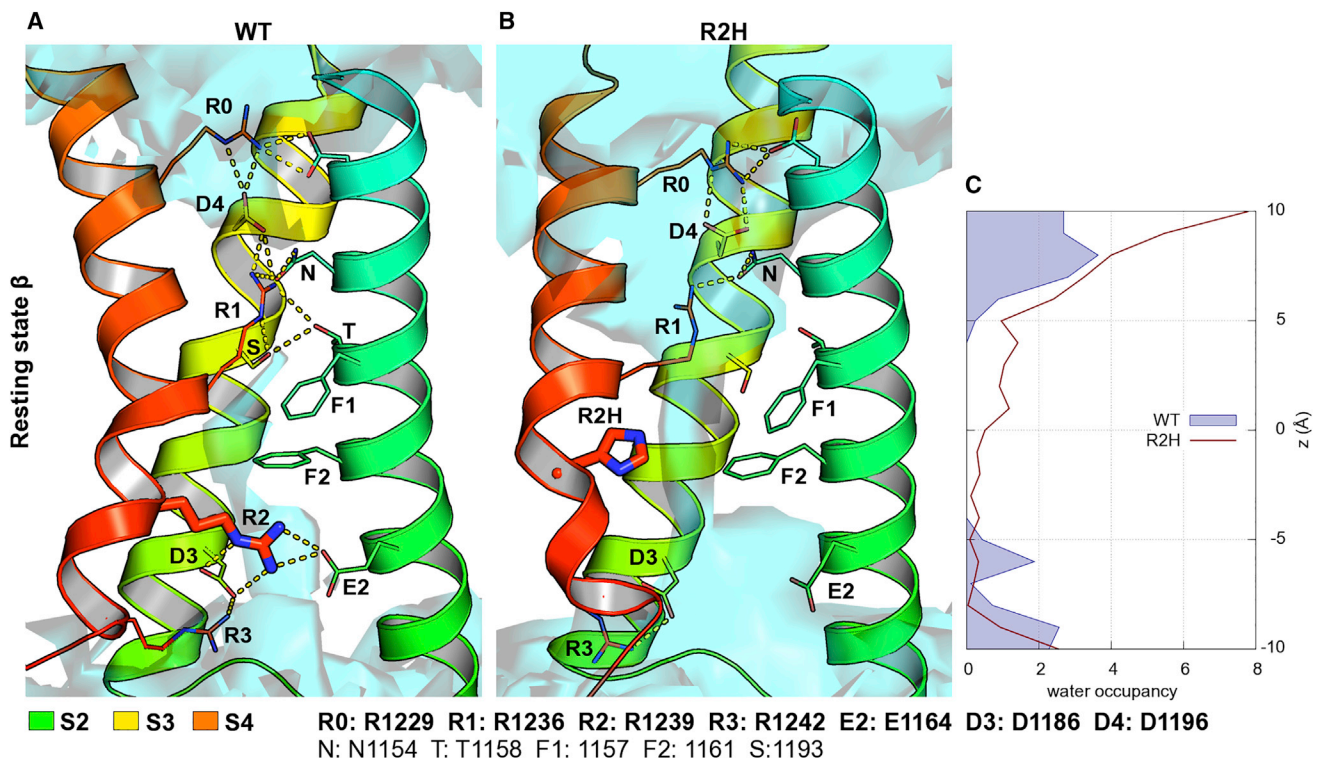

FIGURE 3 Replacement of R2 by His increases VSD water occupancy in IV domain of Ca$_V$1.1 channel in resting state β. (A) Top cluster of WT VSD in resting state β. R0 and R1 interact with several amino acids in S2 and S3 segments, sealing the gating pore from the extracellular space. (B) Mutation of R2 residue to His increases the occupancy of the gating pore by water (*cyan*) as His does not interact with E2, but instead acts as a proton transporter. Furthermore, R1 loses its interaction with D4 and the H-bond network in the upper part of the protein gets weaker, allowing water molecules to enter from the extracellular side. (C) Mutation of R2 to His increases the number of water molecules in the center and upper part of the VSD compared with WT. To see this figure in color, go online.

This causes a longer Cα-Cα distance between R0 and R1, resulting in a charge gap close to D4. Thus, the ionic interaction between R1 and D4 is necessary to stabilize the resting state β.

Upon mutation of Arg to His (R2H), the volume occupied by the side chain of R2 decreased and water molecules replaced the key ionic interactions with E2 and D3 (Fig. 3 B). Moreover, His formed H-bonds with water molecules, acting as proton transporter. The Cα-Cα distances between R2H and E2 or F2 increased from 13.3 to 16.1 Å and from 10.5 to 13.9 Å, respectively, indicating that the S4 helix moves upwards and away from helix S2, generating space for water molecules in the VSD. Moreover, R1 lost its interaction with D4 and the H-bond network in the upper part of the protein became weaker, allowing water molecules to enter from the extracellular side. The water density per frame increased from 4.29 ± 0.37 to 7.55 ± 0.55 in the range −5 to +10 Å along the z axis (Fig. 3 C; Table 1).

Cav1.3 R3H forms a water wire in the resting state β

We next tested if R3H mutation further down the S4 helix can also lead to the formation of a water wire, thus contributing to the predicted gain-of-function phenotype (enhanced aldosterone secretion in APAs (35)). In resting state β, the WT R3 is two helical turns below the conserved Phe (F930) and is surrounded by water molecules (Fig. 4 A). R1 and R2 formed strong salt bridges with negative counter-charges in S2 and S3 helices (Table S4). S2 has an additional Phe residue (F926) that increases the hydrophobic cluster in the center of the VSD and prevents water molecules from entering from the extracellular side.

Upon mutation of the R3 to His, the interaction with E2 is lost. This resulted in a destabilization of the VSD, the inter-helix distances increased (the distance between R1 Cα and D1 Cα is 10 Å in the WT and 12 Å in the mutant), and therefore the constriction in the upper part of the VSD was reduced, allowing water to enter the gating pore (Fig. 4 B). The number of water molecules increased from 0.89 ± 0.07 to 7.28 ± 0.7 in the z axes between −2 and +7 Å (Fig. 4 D; Table 1). Both R1 and R2 side chains changed their positions in the R3H mutant VSD compared with WT VSD. Unlike in the WT, in the R3H VSD the salt bridges formed by R1 with D1 were not always present, allowing water molecules to reach the center of the VSD. The missing charge of R3 was compensated by R2 that replaced R3 in its interaction with E2. Therefore, R2 shares ionic interactions with both E2 and D3, resulting in a weaker H-bond network in the central constriction region. Moreover, our models showed that the His side chain still stayed in the gating pore, making the proton transport even more plausible. Upon VSD activation, the His at R3 reached the hydrophobic constriction plug and formed π-π and cation-π interactions directly with F930 (Fig. 4 C). These interactions, together with the second Phe in S2 (F926), prevented water molecules from reaching and interacting with the His. Therefore, computer structure modeling predicted that the mutant Ca$_V$1.3-R3H channel conducts an ω-current at
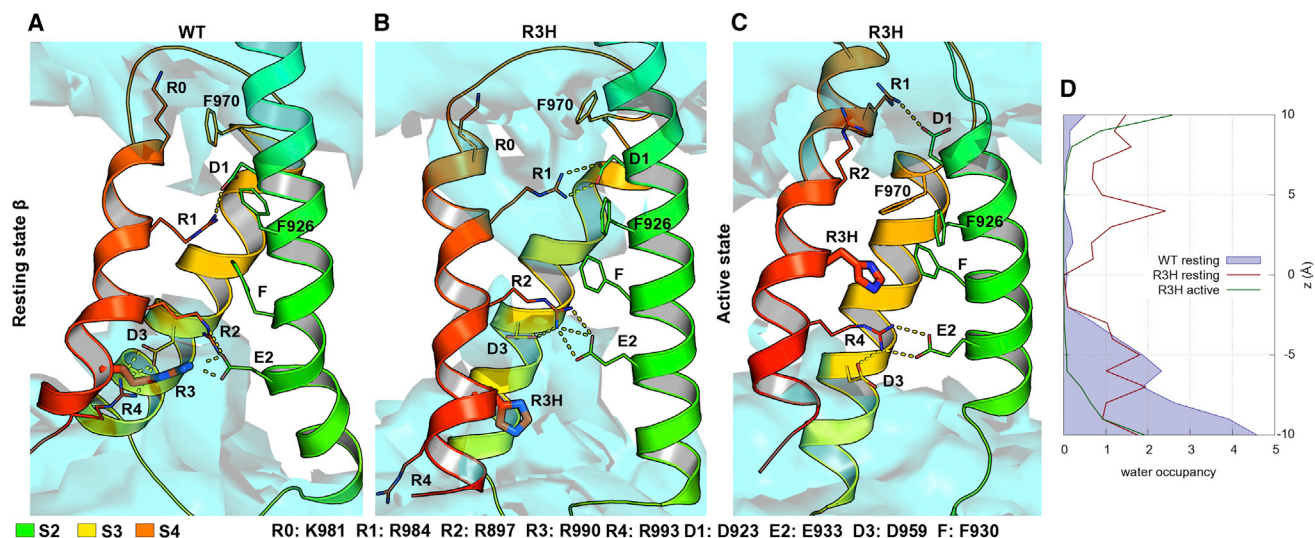

FIGURE 4 Mutation of R3 to His increases water occupancy in III VSD of Ca$_V$1.3 channel in resting state β, but not activated state. (A) Top cluster of WT VSD in resting state β. R1 is oriented upwards and forms ionic interactions with D1 and other polar residues. However, R2 and R3 are oriented downwards and interact with the countercharges E2 and D3. Few water molecules can enter the protein, but no continuous water wire is formed. (B) His at position R3 has no interactions with E2, allowing water molecules to enter from the intracellular side. Moreover, His at position R3 acts as proton transporter as it forms H-bonds with water molecules and moves downwards. (C) In the activated state His at position R3 interacts with F, creating a hydrophobic seal and therefore the water molecules do not enter the gating pore. (D) The R3H VSD has a higher number of water molecules in the resting state β, but not the activated state. To see this figure in color, go online.

resting or hyperpolarized potentials, but not upon channel activation.

Cav1.3 R3H conducts an ω-current at hyperpolarized potentials

Although the presence of ω-currents in the $Ca_V1.1$ gating-pore mutants has been previously reported in a knockin mouse model (27), the $Ca_V1.3$ R3H channel has not been functionally characterized. The expression of the $Ca_V1.3$ R3H channel together with the auxiliary $\alpha_2\delta$-1- and β_3-subunits in tsA-201 cells yielded Ca^{2+} currents with a similar amplitude compared with WT (Fig. 5 A). Mutation of R990 to His in $Ca_V1.3$ resulted in a small, depolarizing shift of the voltage-dependence of activation (Fig. 5 B), but did not alter the voltage-dependence of steady-state inactivation (Fig. S8) or the inactivation kinetics (data not shown). Quantification of the Q_{ON}-gating currents (Fig. 5 C) showed that R3H mutation did not alter the number of channels functionally incorporated in the membrane as the integral of the Q_{ON}-gating currents was not significantly different. Previously it has been shown that substitution of Arg by His or Gly conducts a much larger gating-pore current when guanidinium ions are used as a charge carrier instead of K^+ or Na^+ because guanidinium can pass through the space of the missing guanidine moiety from the Arg side chain (25,61). To test the presence of an ω-pore current, we depolarized the cells from -120 to $+20$ mV (in 20-mV increments) using 165 mM extracellular guanidinium as a charge carrier (Fig. 5 D). Although the expression of WT $Ca_V1.3$ did not increase the inward current more than in the cells lacking the $Ca_V1.3$ α_1-subunit, the currents were significantly increased upon expression of R3H channels at hyperpolarizing (-100 mV), but not depolarized potentials (Fig. 5 E). Depolarization reduced the current through $Ca_V1.3$-R3H to the same levels as in the WT, consistent with our computer structure modeling prediction (Fig. 4 C). The amplitude of the ω-pore current at -100 mV showed a significant correlation with, and the number of channels functionally incorporated in the membrane (Q_{ON}) for $Ca_V1.3$-R3H, but not WT channels (Fig. S9). Furthermore, the $CaV1.3$-R3H ω-pore currents were minimal and indistinguishable from WT at potentials where Ca^{2+} currents through the α-pore is maximal, excluding the possibility that the guanidinium ions pass through the canonical ion-conduction pathway. Taken together, our functional data allows us to conclude that, as structure modeling predicted, the R3H mutation causes ω-currents at hyperpolarizing potentials.

DISCUSSION

Here, we used structure modeling and MD simulations to predict ω-currents in $Ca_V1.1$ and $Ca_V1.3$ channel VSDs
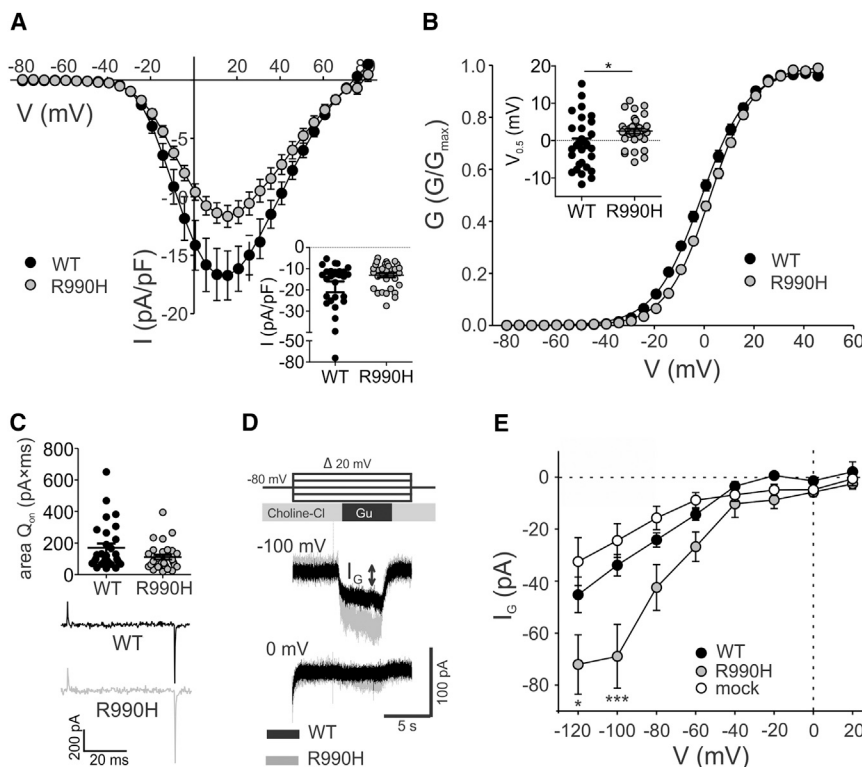

FIGURE 5 Biophysical properties of $Ca_V1.3$ mutant R990H expressed in tsA-201 cells. (A) Current-voltage relationships of WT versus R990H shown as mean $\pm$ SE. Peak current densities illustrated as median with 5–95 percentiles in the inset showed no difference among WT and R990H (median (5–95 percentiles) [pA/pF]: WT: -12.94 ($-58.64/-6.23$), $n = 28$; R990H: -10.79 ($-24.74/-6.03$), $n = 33$; $p = 0.0516$, Mann-Whitney test). Note the break in the y axis, black points mark extreme values. Data were obtained from parallel recordings to account for differences in the expression level between transfections. (B) Steady-state activation curves for WT and R990H shown as mean $\pm$ SE. Mutation R990H resulted in a depolarizing shift of the voltage-dependence of activation (mean $\pm$ SE [mV]: WT: -0.65 ± 1.27, $n = 29$; R990H: 2.61 ± 0.69, $n = 33$; *$p < 0.0231$, unpaired Student's t-test). Half-maximal activation ($V_{0.5}$) shown as mean $\pm$ SEM in the inset. (C) Amplitudes of integrated ON-gating charges (top) and representative ON-gating charges (bottom). Horizontal bars represent mean $\pm$ SEM. WT and mutant channels resulted in similar Q_{ON} suggesting comparable surface expression levels (mean $\pm$ SEM [pA $\times$ ms]: WT: 169.60 ± 27.19, $n = 29$; R990H: 110.70 ± 15.52, $n = 29$; $p = 0.0651$, unpaired Student's t-test). (D) Representative guanidinium currents recorded from cells expressing WT or $Ca_V1.3$-R990H channels. (E) Voltage-dependence of guanidinium currents recorded in mock transfected cells, transfected with WT $Ca_V1.3$ or Ca_V-R990H channel. At hyperpolarizing potentials, the $CaV1.3$-R990H channel conducted significantly more current than WT (mean $\pm$ SEM [pA] at -100 mV: WT: -33.87 ± 4.15, $n = 12$; R990H: -68.95 ± 12.25, $n = 16$; $p < 0.001$, two-way ANOVA with Bonferroni post hoc test).

when one of the first three S4 gating charges harbors a disease-causing mutation. Using site-directed mutagenesis and electrophysiology, we experimentally confirmed that the mutation of R3 charge to His in VSD III of Ca$_V$1.3 channels results in an ω-current at hyperpolarizing potentials. Our study shows that ω-current are state-dependent, but the geometry of the negative countercharges in the VSD, additional positive charges or Phe residues, and the nature of the amino acid that the S4 charge is mutated to dictates the mechanism responsible for the formation of an ω-current and its amplitude. In the Ca$_V$1.1 α_1-subunit, all VSDs have three countercharges, but only two of them are located in conserved positions: E2 in S2 and D3 in S3. The position of the third countercharge responsible for occluding the VSD from the extracellular side varies between odd and even VSDs. In the I and III repeats, the third countercharge (E1 and D1, respectively) is located in helix S2, whereas in the II and IV domains it is placed in helix S3 (E4 in II domain and D4 in IV domain) (Table S3). E1 and D1 occupy the second residue position of helix S2, counting from the extracellular side toward the center of the VSD, whereas E4 and D4 occupy the fourth position in S3. This results in a considerable difference in the distance to the S4 gating charges. This difference in the S4 charge compensation may account for the previously reported differences in the voltage sensitivity and kinetics of the individual VSDs (2,3). Here, we show that the differences in the S4 charge interactions with these countercharges determine the size of the extracellular water-filled vestibule. Another important structure difference is the presence of an additional charge (R0) in the extracellular side of S4 in the III and IV repeats, but not in the II repeat of Ca$_V$1.1. In the absence of interactions formed by R0, the mutation of R1 destabilizes the structure of the VSD, significantly increasing the size of the extracellular vestibule in the II repeat compared with III and IV. Previously, we have shown that neutralization of the R0 charge in the IV VSD of Ca$_V$1.1 did not affect voltage-dependence or amplitude of the Ca^{2+} influx (2), but this study demonstrates the critical functional role of R0 in maintaining the VSD geometry. The presence of an additional Phe residue in the S2 segment of the IV repeat of Ca$_V$1.1 and III repeat of Ca$_V$1.3 also contributes substantially to the water profile in the VSD, as these two WT VSDs display lower water occupancy compared with the II and III Ca$_V$1.1 VSDs. Yet, even in the presence of a second Phe occluding the ω-pore, mutation of S4 charges results in water occupancy through the VSD. Our simulations could also address the important question of whether the nature of the amino acid replacing the S4 charge determines the size of the ω-pore. We found that mutation of the R1 residue in II VSD of Ca$_V$1.1 to Gly or His and to Ser in the III VSD removes the H-bonds that seal the extracellular water-filled vestibule from the core of the VSD. Additionally, the mutation of R1 to Gly but not His or Ser results in a break of the S3 helical structure. Similarly, mutation of R2 in the II

VSD to Ser results in a break and kink of the S4 helix below R2, but not if His replaces R2 in III VSD. These structure alterations do not seem to contribute to the increase of the ω-current in the gating states that we have modeled, but could be responsible for severe alterations of VSD function. In line with this hypothesis, structure models of R1G in II VSD in resting state β were not stable over the 200 ns MD simulations, as the S3 helical structure was completely lost (data not shown). Previous evidence and this study supports the notion that neutralization of positively charged S4 residues creates state-dependent ω-currents. However, does introduction of a charged residue into the VSD have the same functional effect? A noncanonical missense mutation of a noncharged hydrophobic Val residue to negatively charged Glu (V876E) located in the transmembrane segment S3 of the III repeat of Ca$_V$1.1 has also been linked to HypoPP phenotype (62). MD simulation of Ca$_V$1.1-V876E (Fig. S10) showed that exchange of Val 876 by Glu creates a continuous water wire through the VSD in both α- and β-gating states. Replacement of a hydrophobic residue and introduction of a charged residue changes the H-bond interactions in the VSD, allowing water molecules to cross the hydrophobic plug independently of the S4 position.

The S4 mutations characterized in the α_1-subunit of the Ca$_V$1.1 channel have been linked to the HypoPP phenotype characterized by increased intracellular Na$^+$ concentration. Electrophysiological characterization of the Ca$_V$1.1 mutations is controversial because, depending on the experimental conditions and cell system used, the mutation of an S4 charge can result in either a gain-of-function of the α-pore Ca^{2+} current (63) or a loss-of-function (27,64). Nevertheless, it is difficult to directly associate small variations of Ca^{2+} influx with the HypoPP phenotype as the skeletal muscle excitation-contraction coupling relies mostly on sarcoplasmic Ca^{2+} release rather than Ca$_V$1.1 Ca^{2+} influx. Furthermore, other gain-of-function mutations in Ca$_V$1.1 channel outside the VSDs leading to similar alterations in Ca^{2+} influx have been associated with malignant hyperthermia, a potentially lethal autosomal dominant disorder characterized by life-threatening, sustained muscle contractions in response to volatile anesthetics (e.g., halothane) or depolarizing muscle relaxants (65,66). Nevertheless, unless challenged, these individuals are healthy and do not show any skeletal muscle function alterations. Therefore, the cause for the HypoPP phenotype must lie beyond Ca^{2+} current alterations and in fact, for R528H and R1239H Ca$_V$1.1 mutations, a nonselective cation-leak current has been directly or indirectly measured in human skeletal muscle fibers (27,67,68). Although no clear experimental data exist regarding the selectivity of the ω-currents in Ca$_V$ channels, our data demonstrates that water occupies the mutated VSDs, rendering them capable of a cation-leak current. One major difficulty in measuring the ω-currents in mammalian Ca$_V$ and Na$_V$ channels arises from the fact

that, unlike K_V or proton-channels, the Ca_V channels α_1-subunit is a heterotetramer, therefore an S4 mutation affects only one of the VSDs and the ω-current is very small in amplitude. Here, we characterized a $Ca_V1.3$ mutation (R3H) to validate our predictions from our structure modeling. We selected this mutation because, unlike Cav1.1, it can be functionally expressed in tsA-201 cells and its disease-causing mechanism is not obvious from recordings of Ca^{2+} currents. We have previously characterized a number of gain-of-function mutations in $Ca_V1.3$ identified in APAs [35] or individuals with autism spectrum disorders [69], all revealing strong gain-of-function gating changes explaining their disease-causing nature. In contrast, R3H mutation did not show such alterations and minor changes in activity (nonsignificant decrease in current density, minor depolarizing shift of activation voltage, no change in inactivation kinetics), which are compatible with a loss-of-function rather than gain-of-function phenotype. By confirming the existence of an ω-pore at resting membrane potentials, we postulate that $Ca_V1.3$-R3H permits a depolarizing leak current that can gradually increase the resting membrane potential promoting electrical activity and Ca^{2+}-dependent aldosterone production [35]. Taken together, our results demonstrate that mutation of R1, R2, or R3 charges forms ω-pores in Ca_V channels VSDs. Although the mechanism and size of the ω-pores depends on the total number of charges in the S4, the position of the mutated S4 charge or of the countercharges, and the nature of the replacing amino acid, a common feature is that all of the studied mutations result in ω-pores at resting membrane potentials, and therefore have high disease relevance.

SUPPORTING MATERIAL

Ten figures and seven tables are available at http://www.biophysj.org/biophysj/supplemental/S0006-3495(17)30868-8.

AUTHOR CONTRIBUTIONS

S.M., A.L., J.S., P.T., and K.R.L. designed the research. S.M., A.L., A.P., G.N., J.E.F., and F.H. performed the research. S.M. and P.T. wrote the article.

ACKNOWLEDGMENTS

REFERENCES

1. Catterall, W. A. 2010. Ion channel voltage sensors: structure, function, and pathophysiology. *Neuron.* 67:915–928.

2. Tuluc, P., V. Yarov-Yarovoy, …, B. E. Flucher. 2016. Molecular interactions in the voltage sensor controlling gating properties of CaV calcium channels. *Structure.* 24:261–271.

3. Pantazis, A., N. Savalli, …, R. Olcese. 2014. Functional heterogeneity of the four voltage sensors of a human L-type calcium channel. *Proc. Natl. Acad. Sci. USA.* 111:18381–18386.

4. Lacroix, J. J., H. C. Hyde, …, F. Bezanilla. 2014. Moving gating charges through the gating pore in a Kv channel voltage sensor. *Proc. Natl. Acad. Sci. USA.* 111:E1950–E1959.

5. Chanda, B., and F. Bezanilla. 2008. A common pathway for charge transport through voltage-sensing domains. *Neuron.* 57:345–351.

6. Ahern, C. A., and R. Horn. 2005. Focused electric field across the voltage sensor of potassium channels. *Neuron.* 48:25–29.

7. Cannon, S. C. 2015. Channelopathies of skeletal muscle excitability. *Compr. Physiol.* 5:761–790.

8. Jurkat-Rott, K., and F. Lehmann-Horn. 2005. Muscle channelopathies and critical points in functional and genetic studies. *J. Clin. Invest.* 115:2000–2009.

9. Schwaiger, C. S., S. I. Börjesson, …, E. Lindahl. 2012. The free energy barrier for arginine gating charge translation is altered by mutations in the voltage sensor domain. *PLoS One.* 7:e45880.

10. Long, S. B., X. Tao, …, R. MacKinnon. 2007. Atomic structure of a voltage-dependent K+ channel in a lipid membrane-like environment. *Nature.* 450:376–382.

11. Logothetis, D. E., S. Movahedi, …, B. Nadal-Ginard. 1992. Incremental reductions of positive charge within the S4 region of a voltage-gated K+ channel result in corresponding decreases in gating charge. *Neuron.* 8:531–540.

12. Papazian, D. M., L. C. Timpe, …, L. Y. Jan. 1991. Alteration of voltage-dependence of Shaker potassium channel by mutations in the S4 sequence. *Nature.* 349:305–310.

13. Stühmer, W., F. Conti, …, S. Numa. 1989. Structural parts involved in activation and inactivation of the sodium channel. *Nature.* 339:597–603.

14. Starace, D. M., and F. Bezanilla. 2004. A proton pore in a potassium channel voltage sensor reveals a focused electric field. *Nature.* 427:548–553.

15. Sokolov, S., T. Scheuer, and W. A. Catterall. 2005. Ion permeation through a voltage-sensitive gating pore in brain sodium channels having voltage sensor mutations. *Neuron.* 47:183–189.

16. Tombola, F., M. M. Pathak, …, E. Y. Isacoff. 2007. The twisted ion-permeation pathway of a resting voltage-sensing domain. *Nature.* 445:546–549.

17. Gamal El-Din, T. M., H. Heldstab, …, N. G. Greeff. 2010. Double gaps along Shaker S4 demonstrate omega currents at three different closed states. *Channels (Austin).* 4:93–100.

18. Gosselin-Badaroudine, P., L. Delemotte, …, M. Chahine. 2012. Gating pore currents and the resting state of Nav1.4 voltage sensor domains. *Proc. Natl. Acad. Sci. USA.* 109:19250–19255.

19. Moreau, A., P. Gosselin-Badaroudine, …, M. Chahine. 2015. Gating pore currents are defects in common with two Nav1.5 mutations in patients with mixed arrhythmias and dilated cardiomyopathy. *J. Gen. Physiol.* 145:93–106.

20. Struyk, A. F., and S. C. Cannon. 2007. A Na+ channel mutation linked to hypokalemic periodic paralysis exposes a proton-selective gating pore. *J. Gen. Physiol.* 130:11–20.

21. Ramsey, I. S., M. M. Moran, …, D. E. Clapham. 2006. A voltage-gated proton-selective channel lacking the pore domain. *Nature.* 440:1213–1216.

22. Sasaki, M., M. Takagi, and Y. Okamura. 2006. A voltage sensor-domain protein is a voltage-gated proton channel. *Science.* 312:589–592.

23. Tarek, M., and L. Delemotte. 2013. Omega currents in voltage-gated ion channels: what can we learn from uncovering the voltage-sensing mechanism using MD simulations? *Acc. Chem. Res.* 46:2755–2762.

24. Sokolov, S., T. Scheuer, and W. A. Catterall. 2007. Gating pore current in an inherited ion channelopathy. *Nature.* 446:76–78.

25. Tombola, F., M. M. Pathak, and E. Y. Isacoff. 2005. Voltage-sensing arginines in a potassium channel permeate and occlude cation-selective pores. *Neuron.* 45:379–388.

26. Wood, M. L., E. V. Schow, …, D. J. Tobias. 2012. Water wires in atomistic models of the Hv1 proton channel. *Biochim. Biophys. Acta.* 1818:286–293.

27. Wu, F., W. Mi, …, S. C. Cannon. 2012. A calcium channel mutant mouse model of hypokalemic periodic paralysis. *J. Clin. Invest.* 122:4580–4591.

28. Striessnig, J., H. J. Bolz, and A. Koschak. 2010. Channelopathies in Cav1.1, Cav1.3, and Cav1.4 voltage-gated L-type Ca2+ channels. *Pflugers Arch.* 460:361–374.

29. Tricarico, D., and D. C. Camerino. 2011. Recent advances in the pathogenesis and drug action in periodic paralyses and related channelopathies. *Front. Pharmacol.* 2:8.

30. Matthews, E., R. Labrum, …, M. G. Hanna. 2009. Voltage sensor charge loss accounts for most cases of hypokalemic periodic paralysis. *Neurology.* 72:1544–1547.

31. Ophoff, R. A., G. M. Terwindt, …, R. R. Frants. 1996. Familial hemiplegic migraine and episodic ataxia type-2 are caused by mutations in the Ca2+ channel gene CACNL1A4. *Cell.* 87:543–552.

32. Ducros, A., C. Denier, …, E. Tournier-Lasserve. 2001. The clinical spectrum of familial hemiplegic migraine associated with mutations in a neuronal calcium channel. *N. Engl. J. Med.* 345:17–24.

33. Battistini, S., S. Stenirri, …, P. Carrera. 1999. A new CACNA1A gene mutation in acetazolamide-responsive familial hemiplegic migraine and ataxia. *Neurology.* 53:38–43.

34. Kraus, R. L., M. J. Sinnegger, …, J. Striessnig. 2000. Three new familial hemiplegic migraine mutants affect P/Q-type Ca(2+) channel kinetics. *J. Biol. Chem.* 275:9239–9243.

35. Azizan, E. A., H. Poulsen, …, M. J. Brown. 2013. Somatic mutations in ATP1A1 and CACNA1D underlie a common subtype of adrenal hypertension. *Nat. Genet.* 45:1055–1060.

36. Trick, J. L., P. Aryal, …, M. S. P. Sansom. 2015. Molecular simulation studies of hydrophobic gating in nanopores and ion channels. *Biochem. Soc. Trans.* 43:146–150.

37. Biggin, P. C., and P. J. Bond. 2015. Molecular dynamics simulations of membrane proteins. *Methods Mol. Biol.* 1215:91–108.

38. Jensen, M. Ø., V. Jogini, …, D. E. Shaw. 2012. Mechanism of voltage gating in potassium channels. *Science.* 336:229–233.

39. Köpfer, D. A., C. Song, …, B. L. de Groot. 2014. Ion permeation in K$^+$ channels occurs by direct Coulomb knock-on. *Science.* 346:352–355.

40. Vargas, E., F. Bezanilla, and B. Roux. 2011. In search of a consensus model of the resting state of a voltage-sensing domain. *Neuron.* 72:713–720.

41. Ulmschneider, M. B., C. Bagnéris, …, B. A. Wallace. 2013. Molecular dynamics of ion transport through the open conformation of a bacterial voltage-gated sodium channel. *Proc. Natl. Acad. Sci. USA.* 110:6364–6369.

42. Wu, J. P., Z. Yan, …, N. Yan. 2015. Structure of the voltage-gated calcium channel Ca(v)1.1 complex. *Science.* 350:aad2395.

43. Larkin, M. A., G. Blackshields, …, D. G. Higgins. 2007. Clustal W and Clustal X version 2.0. *Bioinformatics.* 23:2947–2948.

44. Molecular Operating Environment (MOE). 2013. Chemical Computing Group Inc., Montreal, QC, Canada.

45. D. A. Case, T. A. Darden., …, P. A. Kollma. 2012. AMBER 12.

46. Simons, K. T., R. Bonneau, …, D. Baker. 1999. Ab initio protein structure prediction of CASP III targets using ROSETTA. *Proteins.* 37:171–176.

47. Tuluc, P., N. Molenda, …, K. Jurkat-Rott. 2009. A CaV1.1 Ca2+ channel splice variant with high conductance and voltage-sensitivity alters EC coupling in developing skeletal muscle. *Biophys. J.* 96:35–44.

48. Jo, S., T. Kim, and W. Im. 2007. Automated builder and database of protein/membrane complexes for molecular dynamics simulations. *PLoS One.* 2:e880.

49. Jorgensen, W. L., J. Chandrasekhar, …, M. L. Klein. 1983. Comparison of simple potential functions for simulating liquid water. *J. Chem. Phys.* 79:926–935.

50. D.A. Case, J. T. Berryman, …, W. a. P. A. Kollman. 2014. AMBER 14.

51. Dickson, C. J., B. D. Madej, …, R. C. Walker. 2014. Lipid14: the amber lipid force field. *J. Chem. Theory Comput.* 10:865–879.

52. Salomon-Ferrer, R., A. W. Götz, …, R. C. Walker. 2013. Routine microsecond molecular dynamics simulations with AMBER on GPUs. 2. Explicit solvent particle mesh ewald. *J. Chem. Theory Comput.* 9:3878–3888.

53. Roe, D. R., and T. E. Cheatham, 3rd. 2013. PTRAJ and CPPTRAJ: software for processing and analysis of molecular dynamics trajectory data. *J. Chem. Theory Comput.* 9:3084–3095.

54. Humphrey, W., A. Dalke, and K. Schulten. 1996. VMD: visual molecular dynamics. *J. Mol. Graph.* 14:33–38, 27–38.

55. Schrödinger, LLC. 2015. PyMOL Molecular Graphics System, Version 1.6. Schrödinger, LLC, New York, NY.

56. Williams, T., and C. Kelley. 2015. Gnuplot 5.0. Samurai Media Limited, Wickford, England.

57. Koschak, A., D. Reimer, …, J. Striessnig. 2001. alpha 1D (Cav1.3) subunits can form l-type Ca2+ channels activating at negative voltages. *J. Biol. Chem.* 276:22100–22106.

58. Ortner, N. J., G. Bock, …, J. Striessnig. 2014. Pyrimidine-2,4,6-triones are a new class of voltage-gated L-type Ca2+ channel activators. *Nat. Commun.* 5:3897.

59. Lieb, A., N. Ortner, and J. Striessnig. 2014. C-terminal modulatory domain controls coupling of voltage-sensing to pore opening in Cav1.3 L-type Ca(2+) channels. *Biophys. J.* 106:1467–1475.

60. Delemotte, L., W. Treptow, …, M. Tarek. 2010. Effect of sensor domain mutations on the properties of voltage-gated ion channels: molecular dynamics studies of the potassium channel Kv1.2. *Biophys. J.* 99:L72–L74.

61. Sokolov, S., T. Scheuer, and W. A. Catterall. 2010. Ion permeation and block of the gating pore in the voltage sensor of NaV1.4 channels with hypokalemic periodic paralysis mutations. *J. Gen. Physiol.* 136:225–236.

62. Ke, T., C. R. Gomez, …, Q. K. Wang. 2009. Novel CACNA1S mutation causes autosomal dominant hypokalemic periodic paralysis in a South American family. *J. Hum. Genet.* 54:660–664.

63. Jurkat-Rott, K., U. Uetz, …, F. Lehmann-Horn. 1998. Calcium currents and transients of native and heterologously expressed mutant skeletal muscle DHP receptor alpha1 subunits (R528H). *FEBS Lett.* 423:198–204.

64. Lapie, P., C. Goudet, …, P. Lory. 1996. Electrophysiological properties of the hypokalaemic periodic paralysis mutation (R528H) of the skeletal muscle alpha 1s subunit as expressed in mouse L cells. *FEBS Lett.* 382:244–248.

65. Pirone, A., J. Schredelseker, …, M. Grabner. 2010. Identification and functional characterization of malignant hyperthermia mutation T1354S in the outer pore of the Cavalpha1S-subunit. *Am. J. Physiol. Cell Physiol.* 299:C1345–C1354.

66. Carpenter, D., C. Ringrose, …, M. A. Shaw. 2009. The role of CACNA1S in predisposition to malignant hyperthermia. *BMC Med. Genet.* 10:104.

67. Jurkat-Rott, K., M. A. Weber, …, F. Lehmann-Horn. 2009. K+-dependent paradoxical membrane depolarization and Na+ overload, major and reversible contributors to weakness by ion channel leaks. *Proc. Natl. Acad. Sci. USA.* 106:4036–4041.

68. Ruff, R. L. 1999. Insulin acts in hypokalemic periodic paralysis by reducing inward rectifier K+ current. *Neurology.* 53:1556–1563.

69. Pinggera, A., A. Lieb, …, J. Striessnig. 2015. CACNA1D de novo mutations in autism spectrum disorders activate Cav1.3 L-type calcium channels. *Biol. Psychiatry.* 77:816–822.